A separated vortex ring underlies the flight of the dandelion

Cathal Cummins,[1, 2, 3] Madeleine Seale,[2, 3, 4] Alice Macente,[2, 4, 5] Daniele Certini,[1]
Enrico Mastropaolo,[4] Ignazio Maria Viola,[1, *] and Naomi Nakayama[2, 3, 6, *]

[1]School of Engineering, Institute for Energy Systems, University of Edinburgh
[2]School of Biological Sciences, Institute of Molecular Plant Sciences, University of Edinburgh
[3]SynthSys Centre for Systems and Synthetic Biology, University of Edinburgh
[4]School of Engineering, Institute for Integrated Micro and Nano Systems, University of Edinburgh
[5]School of Geographical and Earth Sciences, University of Glasgow
[6]Centre for Science at Extreme Conditions, University of Edinburgh

Wind-dispersed plants have evolved ingenious ways to lift their seeds[1,2]. The common dandelion uses a bundle of drag-enhancing bristles (pappus) to help keep their seeds aloft. This passive flight mechanism is highly effective, enabling seed dispersal over formidable distances[3,4]; however, the physics underpinning pappus-mediated flight remains unresolved. Here, we have visualized the flow around dandelion seeds, uncovering an extraordinary type of vortex. This vortex is a ring of recirculating fluid, which is detached due to the flow passing through the pappus. We hypothesized that the circular disk-like geometry and the porosity of the pappus are the key design features that enable the formation of the separated vortex ring. The porosity gradient was surveyed using microfabricated disks, and a disk with a similar porosity was found able to recapitulate the flow behaviour of the real pappus. The porosity of the dandelion's pappus appears to be tuned precisely to stabilize the vortex, while maximizing the aerodynamic loading and minimizing the material requirement. The discovery of the separated vortex ring signals the existence of a new class of fluid behaviour around fluid-immersed bodies that may underlie locomotion, weight reduction, and particle retention of biological and manmade structures.

Dandelions (*Taraxacum officinale* agg.) are highly successful perennial herbs, which can be found in temperate zones all over the world[5]. Dandelions, like many other members of the Asteraceae family, disperse their bristly seeds using the wind and convective updrafts[6,7]. Most dandelion seeds likely land within $2\ \mathrm{m}$[8,9]; however, in warmer, drier and windier conditions, some may fly further (up to $20{,}000$ seeds per hectare travelling more than $1\ \mathrm{km}$ by one estimate)[6,10]. Asteraceae seeds routinely disperse over $30\ \mathrm{km}$ and occasionally even $150\ \mathrm{km}$[3,4].

Plumed seeds comprise a major class of dispersal strategies used by numerous and diverse groups of flowering plants, of which the common dandelion is a representative example. Plumed seeds contain a bundle of bristly filaments, called a pappus, which are presumed to function in drag enhancement (Fig. 1a-c). The pappus prolongs the descent of the seed, so that it may be carried farther by horizontal winds[11], and it may also serve to orientate the seed as it falls[7,12].

Dandelion seeds fall stably at a constant speed in quiescent conditions[2,13–15]. For wind-dispersed seeds, maintaining stability while maximizing descent time in turbulent winds may be useful for long-distance dispersal[16,17]. It is not clear, however, why plumed seeds have opted for a bristly pappus rather than a wing-like membrane, which is known to enhance lift in some other species (e.g., maples[1]). Here, we uncover the flight mechanism of the dandelion, characterizing the fluid dynamics of the pappus and identifying the key structural features enabling its stable flight.

To examine the flow behaviour around the pappus, we built a vertical wind tunnel (Fig. 1d, and M1), designed so that the seed can hover at a fixed height. The flow past the pappus was visualized for both freely flying (Supplementary Video 1) and fixed (Fig. 1e, f, and Supplementary Videos 2 and 3) samples, using long-exposure photography and high-speed imaging. We found a stable air bubble (a vortex ring) that is detached from the body, yet steadily remains a fixed distance downstream of the pappus (Fig. 1e, f, Extended Data Fig. 1a-j, Extended Data Fig. 2a-j, and Extended Data Fig. 3a-d). Bluff bodies (such as circular disks) may generate vortex rings in their wake, but these are either attached to the body or shed from it and advected downstream. The vortex ring in the wake of the pappus is neither attached, nor advected downstream, and thus we named this vortex a Separated Vortex Ring (SVR). The topology of SVRs had been considered theoretically, but was thought to be too unstable to actually occur[18]; here, we show that the pappus's design stabilizes it.

Attached vortex rings form behind circular obstacles; however, it is unclear how the pappus can generate a vortex ring with such a limited air-structure interface (*i.e.*, high porosity). The morphology of the dandelion seeds (M2) was determined using X-Ray Computed Micro-Tomography (μCT, M3) and light microscopy (Fig. 1a-c). The pappus was found to comprise $N = 100\ [95, 106]$ (mean [95% Confidence Interval (CI)], $n = 10$) filaments (Fig. 1a) radiating out from a central point (pulvinus), each with length of $L = 7.41\ [7.35, 7.46]$ mm (mean [95% CI], $n = 937$) (Fig. 1a, b)

*Corresponding author: i.m.viola@ed.ac.uk

*Corresponding author: naomi.nakayama@ed.ac.uk

and diameter of $d = 16.3\,[15.7, 17.0]\ \mu\mathrm{m}$ (mean [95% CI], $n = 10$) (Fig. 1c). The porosity (ϵ, defined as the ratio of the empty projected area to the plan area of the enclosing disk) of the pappus was measured using light microscopy (M4), and was found to be $0.916\,[0.907, 0.923]$ (mean [95% CI], $n = 10$).

The Reynolds number is a non-dimensional parameter characterizing the relative importance of inertial to viscous forces in a fluid. The flow through and around the pappus involves two different Reynolds numbers: that of the entire pappus ($Re = UD/\nu$, where U is the seed's velocity, D is the diameter of the pappus, and ν the kinematic viscosity of the fluid) and that of an individual filament ($Re_\mathrm{f} = Ud/\nu$). Our numerical modelling revealed that the dandelion's pappus benefits from a "wall effect" at low Re_f[19,20] – see M5. Neighboring filaments interact strongly with one another because of the thick boundary layer around each filament, which causes a significant reduction in air flow through the pappus – M7. This effect, which was previously considered to be unimportant for dandelion seeds[2,21], confers the seed's high drag coefficient, which helps the seed remain aloft.

The drag coefficient ($C_D = F/0.5\rho U^2 A$, where F is the drag force acting on the seed, ρ is the density of air, and A is the projected area of the pappus) of the dandelion seeds was calculated by measuring the terminal velocity $U = 39.1\,[34.9, 43]\ \mathrm{cm\,s^{-1}}$ (mean [95% CI], $n = 10$) in a drop test (Fig. 2a). The seeds were ballasted and cut to vary the weight in order to explore a wide range of Re (M6). The mean diameter of the dandelion pappusses in our drop tests was $D = 13.8\,[13.2, 14.3]\ \mathrm{mm}$ (mean [95% CI], $n = 10$). With a mean porosity of $\epsilon = 0.916$, the total projected
area of the pappus is $A = 12.6\,[11.5, 13.5]\ \mathrm{mm^2}$. In order for a solid disk to supply the same drag force (*i.e.*, weight $W = 6.2\,[5.51, 6.86]\ \mu$N (mean [95% CI], $= 10$) of the seed) as the pappus at the same terminal velocity (see M6), its diameter is given by $D_\mathrm{disk} = \sqrt{8W/(1.17\rho\pi U^2)} = 8.6\ \mathrm{mm}$, which is 38% smaller than D. While the Re of the pappus is 357, the equivalent disk has $Re = 222$.

The ratios of the equivalent disk diameter (D_disk) and area (A_disk) to the pappus diameter (D) and area (A), respectively, indicate that the equivalent disk is always smaller but has a significantly higher projected area than the pappus (Fig. 2b). Hence, the pappus delivers more than four times the drag per unit area compared with a solid disk[22], which quadruples C_D. The pappus achieves this effect through the interaction between the thick boundary layers surrounding each filament (M5). In terms of material requirement, the pappus has a volume of less than $77.5\ \mathrm{pm^3}$ (given that individual filaments are more than 50% hollow[15]). An equivalent impervious membrane of this volume would be about $1\ \mu\mathrm{m}$ in thickness, which is far thinner than the wings of flying seeds[14], though material composition may also affect the efficiency of construction.

The existence of the SVR and the elevated drag coefficient are a consequence of the filaments considerably reducing the flow through the pappus, decreasing its permeability. In turn, the pressure downstream of the pappus is reduced, which enhances the drag on the pappus (M7). We measured the flow using Particle Image Velocimetry (PIV, M1 A) in the vortex region of real specimens (Fig. 3a-c); the magnitude of the maximum reverse flow measured was about 10% of the freestream velocity. We distinguished between attached and separated stable vortex rings based on the position of the upstream stagnation point (z_su): if $z_\mathrm{su} > 0$ (see Fig. 3a), the vortex is separated; otherwise it is attached.

In order to explore the effects of porosity, silicon disks mimicking the pappus were microfabricated, varying the degree of the porosity from 0 (*i.e.*, impervious) to 0.92 (comparable to the actual pappus) (M8, and Extended Data Fig. 4a-p). The disks were held fixed in position in the vertical wind tunnel, and flow visualization was used to explore the flow dynamics across the same range of Re as for our biological samples (e.g., Fig. 1g, h). All disks generated a prominent recirculating wake (Fig. 3d-f, and Supplementary Videos 4 and 5). As ϵ increases, this vortex detaches from the disk to form an SVR. The structure and nature of the vortex depends on Re and on ϵ. For low Re, the vortex is axisymmetric, but loses this symmetry as Re increases. This was equally observed on the dandelion pappus (Fig. 1e, f).

Our PIV analysis revealed that the magnitude of the maximum reverse flow for disks is of the order of 10% of the freestream velocity, which is in good agreement with our analysis of the flow around biological samples (Fig. 3a-c). The streamwise length of the SVR is about one characteristic diameter in both the disks and the biological samples.

The SVR is not always steady; for a given porosity ϵ, there is a critical Reynolds number Re_c at which the SVR breaks down into periodic vortex shedding (Extended Data Fig. 5a-l and Supplementary Discussion). We measured Re_c for the dandelion seeds and porous disks (M1 B). For the impervious disk, the measured Re_c (149 ± 2, combined mean $\pm$ s.e.m velocity, diameter and kinematic viscosity measurements) is consistent with existing Direct Numerical Simulations (DNS) results[23,24], therefore validating our experimental methodology.

Identification of Re_c for the disks and dandelion samples (Fig. 4a) revealed that Re_c generally increases with increasing ϵ. Fig. 4a, b show the boundary in the Re-ϵ parameter space that separates regions of steady SVRs and unsteady vortex shedding for porous disks. The mean measured Re_c for dandelion seeds was $Re_c = 429\,[415, 440]$ (mean [95% CI], $n = 10$), which is in good agreement with the value $Re_c = 457 \pm 5$ (combined mean $\pm$ s.e.m velocity, diameter and kinematic viscosity measurements) found for a porous disk of identical porosity (see M1 B). This result indicates that, despite its geometric complexity spreading in height, the pappus acts as if it is a flat circular disk of the same porosity.

All of the dandelion samples tested flew at a Re below Re_c (Fig. 4b). This suggests that evolution has tuned the pappus porosity to eliminate vortex shedding as the seed flies. Thus, the filamentous design of plumed seeds confers two major advantages compared with a membranous one: a four-fold increase in the loading and enhancement of the flight stability. This makes the plumed design far more efficient at flying than a membrane (*i.e.*, a circular disk) for lightweight seeds.

Traditional mathematical models of the dandelion seed's pappus rely on the assumption that each of the seed's filaments can be treated as a translating cylinder, with the total drag on the pappus being the sum of the contributions from each filament[2,14]. However, our numerical modelling and experimental measurements revealed that the flow through the seed entails strong interactions between neighboring filaments[19,20], causing the pappus to behave as a permeable membrane. It has been suggested that changing the permeability of a body could be useful to control or suppress the vortex shedding[25]. A recent study has confirmed that the motion of freely falling disks (with $Re > 10^3$) can be stabilized by a hole in the center of the disk[26]. An oscillating wake is a necessary contributing factor for the unsteady motion of falling disks[26], and the dandelion seed has eliminated this oscillation by evolving a high porosity pappus, thus enabling steady flight.

The initial motion of dandelion seeds is brief but fast, and is rapidly stabilized[15] into an equilibrium orientation that minimizes the seed's terminal velocity, allowing the seed to make maximal use of updrafts[17]. Our experiments demonstrate that the stabilization of plumed seeds is not guaranteed by an arbitrarily porous pappus, as previously believed[11,12]. Instead, stability is gained by tuning the porosity of the pappus.

There are two major types of wind-dispersed seeds, which are distinguished by their appendage (winged or plumed) or equally by their flight mechanism (lift- or drag-based, respectively)[14]. The preferred mode of flight for large seeds, such as the maple seed, is winged[1,2], where high lift forces are attained by a Leading-Edge Vortex (LEV). The LEV reduces the pressure on the upper face of the wing, enhancing the lift compared with non-rotating winged seeds. For winged seeds, greater release heights are necessary to reach the stable lift-generating phase. Therefore, winged flight is probably not effective for the dispersal of small and light seeds of short plants. Instead, the dandelion's bristly pappus enhances its flight capacity via drag using a completely different type of vortex.

The shift from membranous to bristle-based flight occurs in animals, too: very small insects (e.g., *Thrips physapus* L.) have evolved bristly wings rather than membranous ones[20,27–29]. Flight at this scale makes use of a technique called "clap and fling", and bristly wings reduce the force required to fling the wings apart[28,30]. These insects can also float by outspreading their wings, generating 90% of the wing loading of a solid plate with 10% of the material[20]. Bristly appendages are common amongst lightweight fliers and swimmers, and it is likely that the SVR and similar permeability-dependent vortices play a crucial role in their locomotion. They may also underlie the feeding mechanisms of underwater organisms such as the black fly (*Simulium vittatum*) larva, which uses a bristly fan for suspension feeding[31,32]. Because Re_c shifts with the degree of porosity, small changes in the morphology of their appendages may dramatically affect the dynamics of this vortex, leading to a switch in their biological function, for example, from foraging to escape[33].

By uncovering the physics behind the flight of the dandelion, we have discovered a novel type of fluid behaviour around fluid-immersed bodies. As filamentous microstructures within the relevant Re regimes (< 1 for the pore scale and about $100 - 1{,}000$ for the body scale) are commonplace in the biological world[19,31,34], we anticipate that permeability-dependent flow control is prevalent in nature. Traditionally, fluid dynamics investigations tend to observe a single Re scale; exploration of interplays among multiple Re regimes may uncover other as yet unknown fluid behaviour.

[1] Lentink, D., Dickson, W. B., Van Leeuwen, J. L. & Dickinson, M. H. Leading-edge vortices elevate lift of autorotating plant seeds. Science 324, 1438–1440 (2009).
[2] Greene, D. & Johnson, E. The aerodynamics of plumed seeds. Functional Ecology 117–125 (1990).
[3] Ridley, H. N. On the dispersal of seeds by wind. Annals of Botany 19, 351–363 (1905).
[4] Small, J. The origin and development of the Compositæ. New Phytologist 17, 200–230 (1918).
[5] Holm, L. G. World weeds: natural histories and distribution (John Wiley & Sons, 1997).
[6] Tackenberg, O., Poschlod, P. & Kahmen, S. Dandelion seed dispersal: The horizontal wind speed does not matter for long-distance dispersal-it is updraft! Plant Biology 5, 451–454 (2003).
[7] Sheldon, J. & Burrows, F. The dispersal effectiveness of the achene–pappus units of selected Compositae in steady winds with convection. New Phytologist 72, 665–675 (1973).
[8] Nathan, R. et al. Mechanisms of long-distance seed dispersal. Trends in ecology & evolution 23, 638–647 (2008).
[9] Soons, M. B. & Ozinga, W. A. How important is long-distance seed dispersal for the regional survival of plant species? Diversity and Distributions 11, 165–172 (2005).
[10] Greene, D. F. The role of abscission in long-distance seed dispersal by the wind. Ecology 86, 3105–3110 (2005).

[11] Andersen, M. C. An analysis of variability in seed settling velocities of several wind-dispersed Asteraceae. American Journal of Botany 1087–1091 (1992).
[12] Burrows, F. Calculation of the primary trajectories of plumed seeds in steady winds with variable convection. New Phytologist 72, 647–664 (1973).
[13] Andersen, M. C. Diaspore morphology and seed dispersal in several wind-dispersed Asteraceae. American Journal of Botany 487–492 (1993).
[14] Minami, S. & Azuma, A. Various flying modes of wind-dispersal seeds. Journal of theoretical biology 225, 1–14 (2003).
[15] Sudo, S., Matsui, N., Tsuyuki, K. & Yano, T. Morphological design of dandelion (Society for Experimental Mechanics, 2008).
[16] Tackenberg, O., Poschlod, P. & Bonn, S. Assessment of wind dispersal potential in plant species. Ecological Monographs 73, 191–205 (2003).
[17] Stevenson, R. A., Evangelista, D. & Looy, C. V. When conifers took flight: a biomechanical evaluation of an imperfect evolutionary takeoff. Paleobiology 41, 205–225 (2015).
[18] Délery, J. Three-dimensional separated flows topology: singular points, beam splitters and vortex structures (John Wiley & Sons, 2013).
[19] Vogel, S. Life in moving fluids: the physical biology of flow (Princeton University Press, 1981).
[20] Barta, E. & Weihs, D. Creeping flow around a finite row of slender bodies in close proximity. Journal of Fluid Mechanics 551, 1–17 (2006).
[21] Casseau, V., De Croon, G., Izzo, D. & Pandolfi, C. Morphologic and aerodynamic considerations regarding the plumed seeds of Tragopogon pratensis and their implications for seed dispersal. PloS one 10, e0125040 (2015).
[22] Roos, F. W. & Willmarth, W. W. Some experimental results on sphere and disk drag. AIAA journal 9, 285–291 (1971).
[23] Shenoy, A. & Kleinstreuer, C. Flow over a thin circular disk at low to moderate Reynolds numbers. Journal of Fluid Mechanics 605, 253–262 (2008).
[24] Fernandes, P. C., Risso, F., Ern, P. & Magnaudet, J. Oscillatory motion and wake instability of freely rising axisymmetric bodies. Journal of Fluid Mechanics 573, 479–502 (2007).
[25] Cummins, C., Viola, I. M., Mastropaolo, E. & Nakayama, N. The effect of permeability on the flow past permeable disks at low Reynolds numbers. Physics of Fluids 29, 097103 (2017).
[26] Vincent, L., Shambaugh, W. S. & Kanso, E. Holes stabilize freely falling coins. Journal of Fluid Mechanics 801, 250–259 (2016).
[27] Davidi G. & Weihs D. Flow around a comb wing in low-Reynolds-number flow. AIAA Journal 50, 249–253 (2012).
[28] Jones, S. K., Yun, Y. J. J., Hedrick, T. L., Griffith, B. E. & Miller, L. A. Bristles reduce the force required to 'fling' wings apart in the smallest insects. Journal of Experimental Biology 219, 3759–3772 (2016).
[29] Lee, S. H. & Kim, D. Aerodynamics of a translating comb-like plate inspired by a fairyfly wing. Physics of Fluids 29, 081902 (2017).
[30] Santhanakrishnan, A. et al. Clap and fling mechanism with interacting porous wings in tiny insect flight. Journal of Experimental Biology 217, 3898–3909 (2014).
[31] Cheer, A. & Koehl, M. Paddles and rakes: fluid flow through bristled appendages of small organisms. Journal of Theoretical Biology 129, 17–39 (1987).
[32] Ross, D. H. & Craig, D. A. Mechanisms of fine particle capture by larval black flies (Diptera: Simuliidae). Canadian Journal of Zoology 58, 1186–1192 (1980).
[33] van Duren, L. A. & Videler, J. J. Escape from viscosity: the kinematics and hydrodynamics of copepod foraging and escape swimming. Journal of Experimental Biology 206, 269–279 (2003).
[34] Seale, M., Cummins, C., Viola, I. M., Mastropaolo, E. & Nakayama, N. Design principles of hair-like structures as biological machines. Journal of The Royal Society Interface 15 (2018).

Figure 1: The dandelion seed and the vortex that it generates. Structural features of the drag-generating pappus at multi-scales (**a-c**): the μCT scan of a dandelion seed (**a**), the top-down view of the pappus (**b**), and the light microscopy image of a section of a filament (**c**). A vertical wind tunnel (**d**) was used to visualize the steady vortex downstream of a dandelion seed (**e**) at the seed's terminal velocity. At 60% of the terminal velocity, the vortex is slightly larger and more symmetric showing the structure of the separated vortex ring more clearly (**f**). In the same flow conditions as **e** and **f**, solid and porous disks generate vortex shedding (**g**) and a separated vortex ring (**h**), respectively. The scale bars indicate 5 mm, except in **c**, where it denotes 50 μm.

Figure 2: The forces on dandelion seeds compared with those on solid disks. The drag coefficient C_D for natural (red filled circle) and artificially weighted/clipped (black filled circle) dandelion seeds as a function of Re (**a**). The experimental data are a pool of $n = 10$ independent biological samples dropped a total of 55 times. In each of the 55 drops, the weight and velocity was measured multiple times, and the error bars are mean and 95% CI. The blue curve indicates the fit to all of the drop test data. The C_D for a solid disk from previous experiments is also shown (filled square)[22]. The ratios of the equivalent disk diameter to pappus diameter D_{disk}/D (solid magenta curve) and equivalent disk area to pappus area A_{disk}/A (dashed green curve – see insets), showing the dimensions of the impervious disk that generates the same drag as the pappus at the same velocity (**b**). The curves plotted in **b** are obtained entirely from fitting to data in **a**. The shaded area in **a** and **b** spans the range of the biological variation of Re in dandelion seeds.

Figure 3: Flow diagnostics of the SVR for the dandelion seed (**a-c**, representative of $n = 10$ biological replicates) and a circular disk of comparable porosity (**d-f**). Schematic view of the SVR (yellow) and the streamlines (blue) past the pappus (**a**), and above a plan view of the pappus. The origin of the coordinate system $O(r, z)$ is the center of the base of the filaments with the streamwise coordinate z pointing downstream, and the radial coordinate r. The axial velocity u_z was measured along the z (magenta) and r (green) directions with PIV (**b** and **c**, respectively). Note that u_z is nondimensionalized with U, while z and r are nondimensionalized with D. The corresponding figures for disk with porosity 0.89 are presented in (**d-f**), and above a computer aided design drawing of the porous disk in plan view. The data in **e** and **f** were obtained for a single disk.

Figure 4: The loss of stability of the wakes past porous disks and dandelion seeds. The limiting Reynolds Number at which the wake becomes unstable, Re_c, is plotted on the Re-ϵ plane for porous silicon disks (**a**). The mean Re_c for the dandelion samples (green cross), and the literature values[23] for solid disks (magenta triangle). The green data point is mean and 95% CI, $n = 10$ independent biological repeats. Each black dot is data from a single disk at the stated porosity. (**b**) shows a zoomed-in region for $0.8 < \epsilon < 1$, on which the measured values of Re and ϵ for freely flying dandelion seeds (blue crosses) are shown. Blue data are mean and 95% CI, $n = 10$ independent biological repeats. Reynolds number data are identical to that in Fig. 2a. Insets show snapshots of the flow at the indicated Re behind solid disks (left side) and dandelion pappus (right side).

M1. EXPERIMENTS USING VERTICAL WIND TUNNEL

A. Flow visualization

A vertical wind tunnel was built to visualize the flow around natural and artificial (microfabricated) pappuses. Airflow was generated in the wind tunnel using a fan (San Ace 9GA0412P6G001) mounted on the tunnel's inlet. The fan speed was controlled by pulse wave modulation using an Arduino Uno. The flow conditioning consisted of three meshes of open area ratios: 70%, 66%, and 66% respectively, and a honeycomb flow straightener. A fog machine (Rosco 1700) was used to seed the air in the wind tunnel, and the flow was illuminated using a $2.5\,\mathrm{W}$ diode-pumped continuous wave laser (Medialas DPGL 2500) with a wavelength of $532\,\mathrm{nm}$ (Extended Data Fig. 6b).

The videos were obtained using a Canon EOS 70D (for low-speed videos) and a Fastcam Photron SA1 (for high-speed videos) – both with a Tamron $180\,\mathrm{mm}$ F3.5 SP AF Di Macro Lens. The flow speed and turbulent intensity ($T_u = u'/U$, where u' is the root-mean-square of the turbulent velocity fluctuations and U is the mean velocity) was measured using 2D laser doppler anemometry, comprising a $5\,\mathrm{W}$ argon ion laser with a wavelength of $488\,\mathrm{nm}$ and Dantec Dynamics FiberFlow optics (Extended Data Fig. 6a). The mean velocity varied from a minimum of $0.19\,\mathrm{m\,s^{-1}}$ to a maximum of $0.72\,\mathrm{m\,s^{-1}}$, with a maximum T_u of 3.6% and a mean T_u of 2.3%. The flow past $n = 10$ dandelion seeds – randomly selected from ten different capitula (M2) – flying at their terminal velocity was visualized in the wind tunnel; each seed showed a prominent SVR in its wake (Supplementary Video 1).

The same ten seeds that were used for the freely flying experiments were fixed to trestles, and held fixed in the wind tunnel at different flow speeds; long exposure photographs of the flow past these seeds were obtained using a Canon EOS 70D. Downstream of each seed, an SVR is present, which is stable across the entire biological variation of the seeds (Fig. 1e, f).

Particle Image Velocimetry (PIV) was performed using the CW laser to illuminate air that is seeded with smoke, and a high-speed camera; the data were post-processed using the MATLAB toolbox PIVlab 1.41. The frame rate used in the PIV experiments varied from a minimum of 50 fps (for low flow-speed experiments) to a maximum of 250 fps (for high flow-speed experiments). We used a multipass linear window deformation technique: the first pass used a 64×64 pixel interrogation window, the second pass 32×32 pixel interrogation window and sub-pixel displacement was estimated using two-dimensional Gaussian regression. Since we were interested in the flow far from the body, masking was not necessary, and hence, no masking was used.

B. Detection of vortex shedding

The detection of vortex shedding from dandelion samples and replica pappuses in the wind tunnel experiments was measured using MATLAB to compute the structural similarity index between a reference frame of the wake region and subsequent frames of the video[35,36].The power spectral density estimate of this signal was then found using the covariance method, and the peak frequency f was extracted, for a range of Re. A non-zero f signalled the presence of vortex shedding. In order to compute Re_c for our dandelion seeds, we analyzed the flow past $n = 10$ seeds, which were fixed in our wind tunnel. We found that the 95% confidence interval for the mean Re_c for the dandelion samples was $Re_c = 429\ [415, 440]$ (mean [95% CI], $n = 10$).

In order to compare the mean Re_c for dandelion samples to the value of Re_c predicted by our porous disks, we linearly interpolated between the data points in Fig. 4b. From this, we estimated that Re_c for porous disks at the same porosity as our dandelion samples is $Re_c = 457 \pm 5$ (combined mean $\pm$ s.e.m velocity, diameter and kinematic viscosity measurements) (Fig. 4a, b).

M2. GROWTH OF DANDELION SPECIMENS (*TARAXACUM OFFICINALE AGG.*)

Dandelion seeds were collected from a single plant growing in Edinburgh ($55.922684, -3.170703$) in April 2014. Seeds were germinated in $10\,\mathrm{cm}$ round Petri dishes containing distilled water in 16 h light/ 8 h dark conditions ($100\,\mu\mathrm{mol\,m^{-2}\,s^{-1}}$ 25℃ day, 23℃ night) for 2 weeks. They were then transplanted to $7 \times 7 \times 8\,\mathrm{cm}$ pots with soil/perlite mix 60% v/v Levington's F2+S (Everris), 24% v/v standard perlite (Sinclair), 16% v/v washed horticultural sand $0.3\,\mathrm{g\,L^{-1}}$ Exemptor (Everris)) and grown in 16 h light/8 h dark conditions in a controlled environment room ($100\,\mu\mathrm{mol\,m^{-2}s^{-1}}$, 21℃) for 4 weeks. Plants were transplanted into $4\,\mathrm{L}$ pots with peat/sand mix (83% v/v medium peat (Clover), 21% v/v washed horticultural sand, $3\,\mathrm{g\,L^{-1}}$ garden limestone (Arthur Bowers), $1\,\mathrm{g\,L^{-1}}$ Osmocote Exact Standard 5-6 months (Everris), $0.4\,\mathrm{g\,L^{-1}}$ Exemptor (Everris)) and transferred to a glasshouse with ambient light supplemented to ensure a 16 h day (minimum intensity of $250\,\mu\mathrm{mol\,m^{-2}s^{-1}}$, 06:00 – 22:00 GMT) and temperature of 21℃ day, 18℃ night. For μCT scans, seeds used were the offspring of the original collected plants.

For all other experiments, seeds were from the following generation. All of these seeds from the second generation originated from the same parent plant. As *T. officinale* is apomictic, all seeds are assumed to be genetically identical. Throughout the paper, we use the term dandelion "seed" as a shorthand to refer to the entire diaspore (fruit-pappus unit).

M3. X-RAY COMPUTED MICROTOMOGRAPHY (μCT)

Ten dandelion samples were individually attached using forceps to machined sharpened carbon cones with cyanoacrylate glue (RS Pro). Samples were sputter coated with gold for $100 - 200$ s (corresponding to a thickness of approximately $150 - 300$ nm). Scan settings were as shown in Extended Data Tab. 1.

Data were reconstructed using Octopus 7 software[37]. The voxel (3-dimensional pixel) size of the reconstructed μCT datasets was 25 μm.

Post-processing of the reconstructed data was carried out with Avizo 9.0.1 (FEI, ThermoFisher Scientific) and R[38] – see Extended Data Fig. 7 for the workflow chart. Scans were filtered by unsharp masking with a 3 voxel kernel size. Small holes of up to 26 voxels were filled and a labeled image was created by interactive thresholding.

For analysis of the pappus geometry, the segmented data were skeletonized using an implementation of the TEASAR algorithm[39] (scale $= 2.5$, constant $= 4$) in which a tree structure is formed from traced peaks of distance maps and looping is not permitted. The starting point for skeletonization was manually selected for each sample to begin at the central point of the pappus (the pulvinus, where all filaments are attached). Nodes with a co-ordination number of one (*i.e.*, connected to no more than one other node) were considered potential filament end points and nodes were visually inspected to remove false positives from further analysis. A coordinate mapping of each filament was obtained by finding the shortest path between the central starting point and each filament end.

The point co-ordinates along the length of each filament were smoothed using a Gaussian smoothing filter (window size $= 16$, alpha $= 2.5$, tails retained). The window size was selected by stepwise increases of the window size until the mean filament arc length changed by less than 1% from its previous value (*i.e.*, interpolation between co-ordinates of the centerline was no longer significantly affected by noise arising from the limited pixel resolution of the scan). The co-ordinates of each spatial dimension were separately smoothed with the same settings. Points corresponding to a central disk (the pulvinus) onto which the filaments are attached were removed from further analysis (by removing a central sphere of $0.56 - 0.64$ mm radius depending on the sample) such that only filaments themselves were included.

The spacing between filaments in the pappus was estimated by calculating the distance of the centerline of each filament from its nearest neighboring filament centerline. 93.5% of filaments were correctly segmented, skeletonized and included in the analysis. Spacing was found to linearly increase from zero at the pulvinus to 1.32 mm at the edge of the pappus. This maximum distance divided by two represents the mean distance between filaments, and was an input into the numerical model (M5). As a small number of filaments were not included, the nearest neighbor calculations represent a slight overestimate. Additionally, it is important to note that these spacing distances are the spacing between centerlines. Filament diameters were at the limit of the resolution of the CT scanner so they were not calculated from this data.

M4. MICROSCOPY

A. Light microscopy: Individual filament

All filaments except one were removed from each dandelion fruit. The stalk and pulvinus were stuck onto a glass slide with a small piece of modelling clay such that the single remaining filament lay flat on the slide. Images were acquired with a Nikon E600 fluorescent microscope using a $10\times$ objective, 1 ms exposure, 0.6 gamma and $2\times$ gain. Each field of view was imaged 1-8 times at different focal (Z) planes to account for slight changes in topography. Image processing was carried out in ImageJ to calculate filament diameters[40]. Sharp composite images were obtained for each field of view by model-based deconvolution, stitched together with linear blending and converted into binary images[41,42]. Distance maps were computed and the skeletonized centerline of the filament was overlaid. Diameters were calculated from the distance map at each pixel along the centerline of the filament. The mean of the diameter values at all points along the filament was calculated to give an overall filament diameter. Error in diameter values due to binarization was ± 0.80 μm based on a pixel size of 0.40 μm.

B. Light microscopy: Entire pappus

The porosity of $n = 10$ dandelion seeds was measured using light microscopy. First, the mean diameters of dandelion pappuses D were measured using a Dino-Lite digital microscope, which was found to be $D = 13.8\ [13.2,14.3]$ mm (mean $[95\%\ \text{CI}]$, $n = 10$). The porosity of these pappuses was then measured. The images were obtained using a Nikon SMZ1500 stereomicroscope, with: $1\times$ magnification, 38.5 ms exposure, 0.6 gamma, $1.0\times$ gain and 1.60 saturation. The pappuses were placed on the glass slide covered with $5\ \mu$L of 99% Ethanol and a glass coverslip. Overlapping sections of each pappus were imaged at different positions on the focal plane to account for the entirety of the pappus. These images were stitched together with linear blending[42] in ImageJ to form the entire pappus image. The pulvinus was inscribed in a circle to find the center of the pappus. Images, converted to RGB color format, were used to calculate the empty area inside the disk, applying a color threshold. The porosity p of the flattened sample was obtained by calculating the ratio of empty area to the total plan area of the pappus. The porosity ϵ of the original sample was then calculated to be $\epsilon = 1 - 2L(1-p)/D = 0.916\ [0.907, 0.923]$ (mean $[95\%\ \text{CI}]$, $n = 10$)[2].

C. Error analysis: Different magnifications

A single filament was removed from a dandelion fruit and placed on a glass slide. The porosity of a rectangular field of view including a section of the filament was measured at four different magnifications. From this, the error due to the finite resolution of the equipment was estimated to be 0.54%.

M5. CREEPING FLOW PAST AN ARRAY OF FILAMENTS

The Reynolds number $Re = UD/\nu$ is calculated using the pappus diameter D as the characteristic dimension, and was found to be of the order of 400. Note however, that when discussing low-Re effects, a filament Reynolds number, based on a filament's diameter ($Re_\text{f} = Ud/\nu = 0.422$) is used. Since $Re_\text{f} < 1$, the equations for Creeping flow apply, and may be used to investigate the flow past the pappus. Consider the low Reynolds number flow past a body: it is well known that the velocity boundary layer attached to the body extends many body diameters into the fluid[43], influencing the flow far from it. When this flow interacts with distant boundaries, it is known as a "wall effect". Reference 19 provides the following estimate of when this effect can be ignored:

$$\frac{y}{l} > \frac{20}{Re_\text{f}}$$

where l is the characteristic dimension of the body and y is the distance to the nearest boundary. In the case of the dandelion, we are considering the effect of neighbouring filaments, so $l = 16.3\ \mu$m, $Re_\text{f} = 0.422$, and y is the mean distance between the filaments (see M3). In order to neglect the influence of neighboring filaments, we can estimate that filaments should be spaced greater than 47 filament diameters apart. However, based on our μCT scan data (M3), the mean distance between the filaments is about 41 filament diameters, hence the effects of neighboring filaments cannot be ignored.

To further confirm this hypothesis, we computed the slow flow (velocity vector $\boldsymbol{u}$ and pressure p) past a rectangular array of 100 filaments of diameter and length equal to that of the dandelion seeds. The filaments within the array were separated a distance equal to the mean distance between the filaments. We adopted the modelling approach in ref. 20. The creeping flow equations

$$\nabla p = \mu \nabla^2 \boldsymbol{u}$$

$$\nabla \cdot \boldsymbol{u} = \boldsymbol{0}$$

were solved in the fluid domain (μ is the dynamic viscosity of the fluid), with each filament represented by a distribution of singularities (Stokeslets with intensity α_i and Doublets with intensity β_i) along its axis.

The intensities of the singularities are computed using Wolfram Mathematica 11 by solving an appropriate system of linear equations. We used 64 points uniformly distributed along the axis of each body. Once the equations have been solved for $\boldsymbol{u}$ and p, the drag on each member of the pappus can be computed.

The drag exerted on the ith filament can be expressed in terms of the integral of the Stokeslet intensity along the length of the filament as follows:

$$D_i = 8\pi\mu \int_0^L \alpha_i(s)\, ds\,, \quad i = 1, \ldots m.$$

In Extended Data Fig. 8d, the drag on each filament divided by the drag of a single, isolated filament[44] D_i/D_0 is plotted. We found that there is a strong interaction between filaments. On average, a filament within the pappus experiences an 84% reduction in the drag, compared with an isolated filament. This indicates that the pappus is behaving somewhat like a continuous surface, significantly reducing the airflow through it. The blockage effects resulting from air being pushed around the pappus are not captured by this model. Hence, this model cannot be used to explore the resulting flow field around the pappus.

Strictly speaking, this model is valid in the limit as Re_f tends to zero. However, since Re_f is finite, some errors are introduced[31]. Here, we examine the error introduced by neglecting the small but finite Re_f for the dandelion's filaments. In ref. 27, the slow flow past an array of slender bodies was examined using computational fluid dynamics for a range of small to moderate Re_f, ranging from 0.01 to 100. This parametric study found that for $Re_\mathrm{f} \leq 1$ and spacing of 10 filament diameters, the flow speed between adjacent filaments are identical to that found in the Stokes flow model in ref. 20. The drag force computed using the model of ref. 20 differed from that computed in ref. 27 but the trend and order of magnitude remained very similar.

M6. MEASUREMENTS OF C_D

The terminal velocity U of $n = 10$ dandelion seeds selected randomly from different plants was measured by dropping each seed five times. A DSLR camera (Canon EOS 70D) recorded the fall at 50 fps over 1 m. The position of the seeds was tracked using MATLAB, and the terminal velocity U was found using linear regression of the tracked position data.

Additional masses (strand of polyvinylesiloxane impression material) were attached to the seeds, and the terminal velocity of the composite mass was measured as described above. The mass (seed + strand) m was measured using a Mettler AE 240 analytical balance. In order to explore the terminal velocity for masses less than a seed's natural mass, a small part of the seed was cut, and the terminal velocity of this was measured as described above.

The drag coefficient C_D was computed using

$$C_D = \frac{mg}{0.5\rho A U^2},$$

where $\rho = 1.204\ \mathrm{kg\,m^{-3}}$ is the density of air at normal temperature and pressure, $g = 9.81\ \mathrm{m\,s^{-2}}$ is the acceleration due to gravity, and A is the total projected area of the pappus. By adding masses, the variation of C_D across a wide range of Reynolds numbers $Re = UD/\nu$, where $\nu = 15.11 \times 10^{-6}\ \mathrm{m^2 s^{-1}}$ is the viscosity of air and D is the pappus diameter, was explored.

The mean mass of the dandelion seeds in our experiments was $0.633\ [0.562, 0.699]$ mg (mean [95% CI], $n = 10$), and the seeds fell at an average speed of $U = 39.1\ [34.9, 43.0]\ \mathrm{cm\,s^{-1}}$ (mean [95% CI], $n = 10$), leading to a mean of $Re = 357$.

M7. FLOW FIELD CHARACTERIZATION OF THE SVR

In order to characterize the SVR, we performed DNS of the flow past a permeable circular disk with aspect ratio $\chi = d/D = 0.0011$, Darcy number $Da = k/D^2 = 4.7 \times 10^{-6}$, and porosity $\epsilon = 0.916$ at $Re = UD/\nu = 175$, where k the permeability of the disk, and U is the freestream speed (values for porosity and diameter obtained from morphological analysis of samples – see Extended Data Tab. 2). We adopted the modelling approach of ref. 25, where we considered the steady, axisymmetric flow past the permeable disk. In the fluid domain, the steady-state Navier-Stokes equations are solved and inside the permeable disk, the steady-state Darcy-Brinkmann equations are solved. Continuity of the velocity and pressure are enforced at the boundary between the fluid and porous domains, and the discretized system of equations is solved using COMSOL Multiphysics.

The results from our numerical modelling are shown in Extended Data Fig. 8. The flow around and through the porous disk is characterized by a significant slow down of velocity u_z (Extended Data Fig. 8a). This is associated with a pressure increase upstream of the disk (Extended Data Fig. 8b). Across the disk, the flow velocity is conserved while the disk subtracts potential energy from the flow, resulting in a lower pressure downstream. Subsequently, the slow flow downstream of the disk is affected by the adverse pressure gradient between the high pressure in the far field and the low pressure in the region downstream of the disk. This pressure gradient further slows down the flow, which is eventually led to reverse and form a recirculation bubble due to viscous effects (Extended Data Fig. 8a, c). Further downstream, the gradual pressure recovery enables a lower pressure gradient, *i.e.*, a lower pressure force on the fluid, which hence recovers its velocity by entrainment of momentum from the adjacent flow streams. This results in an asymptotic increase of velocity towards the far field. We quantified the numerical uncertainty U_num, which is the sum of the uncertainties due to the grid (U_g) and the iterative convergence (U_c) using the approach adopted by previous authors[45]

We found that the numerical uncertainty in the computed value of streamwise length of the SVR, was $U_{\mathrm{num}} < 0.02\%$ for the value of Re, Da, and ϵ considered in this study.

The results from this numerical model provide insight into the pressure field and the general flow structure around the pappus. However, there are limitations to this simple model. The assumption of axisymmetry precludes any investigation of the observed symmetry breaking of the vortex (similar symmetry breaking is observed for impervious disks[23]) or the breakdown of the SVR into vortex shedding at higher Re. In the latter case, in order to compute Re_c using this model, the assumption of time independence would also have to be relaxed.

A. Topology of the SVR

Topologically, the SVR is a degenerate focus with half-saddle separation (z_{su}) and reattachment (z_{sd}) points. For low Re, the vortex is axisymmetric, however at some Re_c, the steady SVR loses its azimuthal symmetry by a regular bifurcation as illustrated in the schematic diagram Extended Data Fig. 3e,f. The subsequent breakdown in stability of the SVR at $\mathrm{Re} = \mathrm{Re}_c$ is likely to occur through a Hopf bifurcation[24].

M8. DESIGN AND MICROFABRICATION OF REPLICA PAPPUSES

Replica pappuses of various porosities were designed using Wolfram Mathematica: first, a rectangle with length l mm and varying widths w was created using the rectangle function. The rectangle was then copied and rotated around a central point 20 times using the Mathematica function GeometricTransformation to create a replica pappus with $n = 42$ filaments. The porosity of the disk depended on the width of the filament according to

$$\epsilon = 1 - \frac{nw\{(l-b)+b/2\}}{\pi l^2},$$

where $b = w/(2\tan(\pi/n))$. The resulting design was exported as a vector image for use in the microfabrication process. The length l was 10 mm (to explore the region $Re < 170$) and 14 mm (to explore $Re > 170$).

The replica pappuses were manufactured using photolithography and microfabrication techniques. A $1\ \mu$m thick layer of silicon oxide (SiO_2) was grown on a 3 inch silicon wafer substrate (thickness of $380\ \mu$m). After spin coating a $7\ \mu$m thick photoresist film on the SiO_2 layer, the dandelion designs were patterned photolithographically on the substrate. Afterwards, the exposed SiO_2 was removed by reaction ion etching in a plasma formed of CHF_3 and Ar. At this point, the dandelion structure was etched in deep reactive ion etching (Bosch process) using the photoresist and SiO_2 layer as an etch mask. Once the wafer was etched through completely, the dandelion structures was rinsed and bonded to an artificial stem to allow for testing in the vertical wind tunnel.

M9. STATISTICS

Throughout the paper, the 95% confidence intervals are obtained using bias-corrected and accelerated bootstrapping. All of the morphological data obtained from our dandelion samples was shown to be normally distributed, apart from the length filament L.

M10. DATA AVAILABILITY

The datasets generated during and/or analyzed during the current study are available from the corresponding author upon reasonable request.

M11. CODE AVAILABILITY

The codes used to produce Fig. 4a are available at Edinburgh DataShare (DOI:10.7488/ds/2362 and DOI:10.7488/ds/2363) [35,36].

[35] Cummins, C., Viola, I. M., Mastropaolo, E. & Nakayama, N. Matlab scripts for analysis of vortex shedding (2018). URL http://dx.doi.org/10.7488/ds/2362.

[36] Cummins, C., Viola, I. M., Mastropaolo, E. & Nakayama, N. Vortex shedding in the wake of a 75% porous disk (2018). URL http://dx.doi.org/10.7488/ds/2363.

[37] Dierick, M., Masschaele, B. & Hoorebeke, L. V. Octopus, a fast and user-friendly tomographic reconstruction package developed in LabView®. Measurement Science and Technology 15, 1366 (2004).

[38] R Core Team. R: A Language and Environment for Statistical Computing. R Foundation for Statistical Computing, Vienna, Austria (2013).

[39] Sato, M., Bitter, I., Bender, M. A., Kaufman, A. E. & Nakajima, M. TEASAR: Tree-structure extraction algorithm for accurate and robust skeletons. In Computer Graphics and Applications, 2000. Proceedings. The Eighth Pacific Conference on, 281–449 (IEEE, 2000).

[40] Schneider, C. A., Rasband, W. S. & Eliceiri, K. W. NIH Image to ImageJ: 25 years of image analysis. Nature methods 9, 671–675 (2012).

[41] Forster, B., Van De Ville, D., Berent, J., Sage, D. & Unser, M. Complex wavelets for extended depth-of-field: A new method for the fusion of multichannel microscopy images. Microscopy research and technique 65, 33–42 (2004).

[42] Preibisch, S., Saalfeld, S. & Tomancak, P. Globally optimal stitching of tiled 3D microscopic image acquisitions. Bioinformatics 25, 1463–1465 (2009).

[43] White, C. M. The Drag of Cylinders in Fluids at Slow Speeds. Proceedings of the Royal Society of London A: Mathematical, Physical and Engineering Sciences 186, 472–479 (1946).

[44] Chwang, A. T. & Wu, T. Y.-T. Hydromechanics of low-Reynolds-number flow. Part 2. Singularity method for Stokes flows. Journal of Fluid Mechanics 67, 787–815 (1975).

[45] Viola, I., Bot, P. & Riotte, M. On the uncertainty of CFD in sail aerodynamics. International Journal for Numerical Methods in Fluids 72, 1146–1164 (2013).

Acknowledgements

This work was supported by the Leverhulme Trust [RPG-2015-255] and the Royal Society [UF140640]. We thank Dr Ian Butler (Geosciences, University of Edinburgh) for their assistance in the CT scan, and Dr Andrew Firth and Mark Mason (Engineering, University of Edinburgh) in the building of the wind tunnel.

Author Contributions

CPC, EM, IMV and NN designed the experiments. CPC designed and set up the wind tunnel. CPC carried out the numerical analyses and the flight assay and flow visualization with assistance from MS and DC. CPC designed and EM fabricated the silicon disks. AM optimized and performed the CT scan, and MS analyzed the resulting 3D images. CPC wrote the manuscript, with help from MS, EM, IMV and NN in revision and editing. EM, IMV and NN designed and oversaw the project; IMV supervised the fluid mechanics investigations, and NN the biological and structural studies.

Competing interests

The authors declare no competing interests.

Extended data

Extended Data Tab. 1: μCT scan acquisition settings.

Extended Data Tab. 2: Morphological data (mean [95%CI], n) of dandelion seeds.

Extended Data Fig. 1: SVR visualization in the wake of 10 fixed dandelion seeds (flow speed is one half the seeds' terminal velocity). Each image taken using long-exposure photography.

Extended Data Fig. 2: SVR visualization in the wake of 10 freely flying dandelion seeds. Each image corresponds to a snapshot from a video of the dandelion's flight in the wind tunnel. The images show the seeds as they pass through the laser sheet, and the SVR may be difficult to identify in some panels because of the orientation of the laser sheet with respect to the axis of the SVR.

Extended Data Fig. 3: The breakdown in symmetry in the SVR of dandelion seeds. At low speeds, the SVR is axisymmetric (**a** is contrast enhanced, original image **b**). At higher speeds, this symmetry is lost (**c** is contrast enhanced; original image **d**). The experiments in **a-d** were repeated independently on $n = 10$ biological samples, with similar results. The axisymmetry of SVR at low Re (**e**) breaks down at higher Re (**f**).

Extended Data Fig. 4: Images of porous disks showing the resolution of the technique for disks of various porosities. (**a-b**) Impervious disk. (**c-f**) 33% Porous disk. (**g-h**) 55% Porous disk. (**i-j**) 75% Porous disk. (**k-p**) 89% Porous disk.

Extended Data Fig. 5: Steady and unsteady wake behind porous disks and pappuses video snapshots. The top row shows the flow visualization behind a solid disk, with a steady wake (**a**) and an unsteady wake at three time points within one period of vortex shedding (**b-d**). Similarly, the middle row shows the flow around a porous disk ($\epsilon = 0.75$) with a steady wake (**e**) and an unsteady wake at three time points within one period of vortex shedding (panels **f-h**). The bottom row shows the wake behind a dandelion sample with a steady SVR (**i**) and at three time points within one period of vortex shedding (panels **j-l**).

Extended Data Fig. 6: The experimental setup for laser doppler anemometry and flow visualization. A schematic drawing of the experimental setup for laser doppler anemometry to measure the flow speed and turbulent intensity in the wind tunnel (**a**) and the experimental setup for flow visualization in the wind tunnel using a CW laser and high-speed camera (**b**). Photograph of the actual experimental setup for flow visualization (**c**).

Extended Data Fig. 7: Workflow for post-processing of the μCT scan data.

Extended Data Fig. 8: The flow past a porous disk using direct numerical simulations and boundary integral methods. The axial velocity u_z/U (**a**), pressure $p/\rho U^2$ (**b**), and streamlines (**c**), showing the presence of an SVR with upstream and downstream stagnation points z_{su} and z_{sd} respectively. The reduction in the drag force on filaments within an array moving at slow speeds (**d**), as calculated using a boundary integral method. The force D_i on the ith filament of a rectangular pappus, divided by the drag force for an isolated filament D_0.

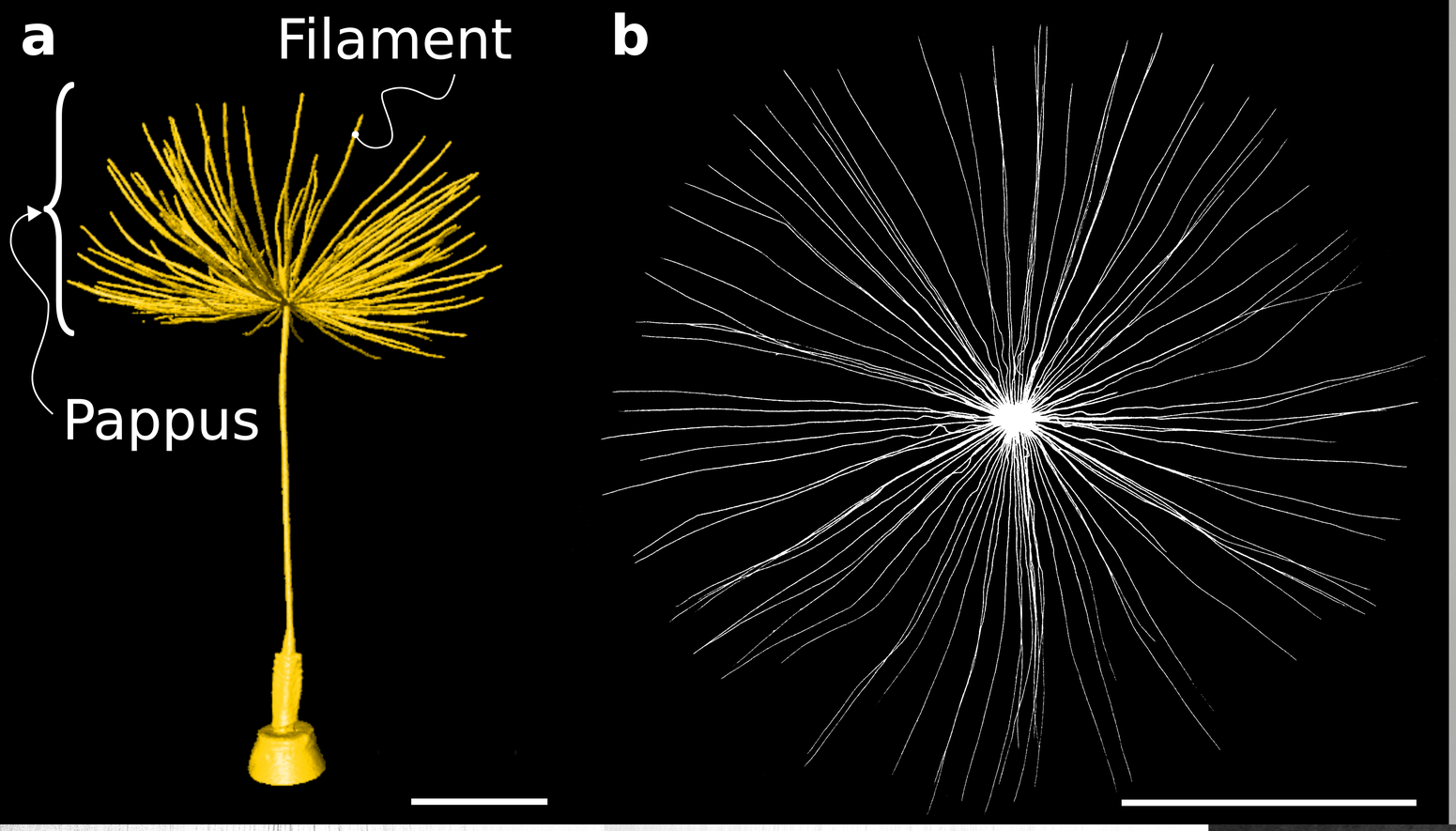
a
Filament
Pappus

b

c

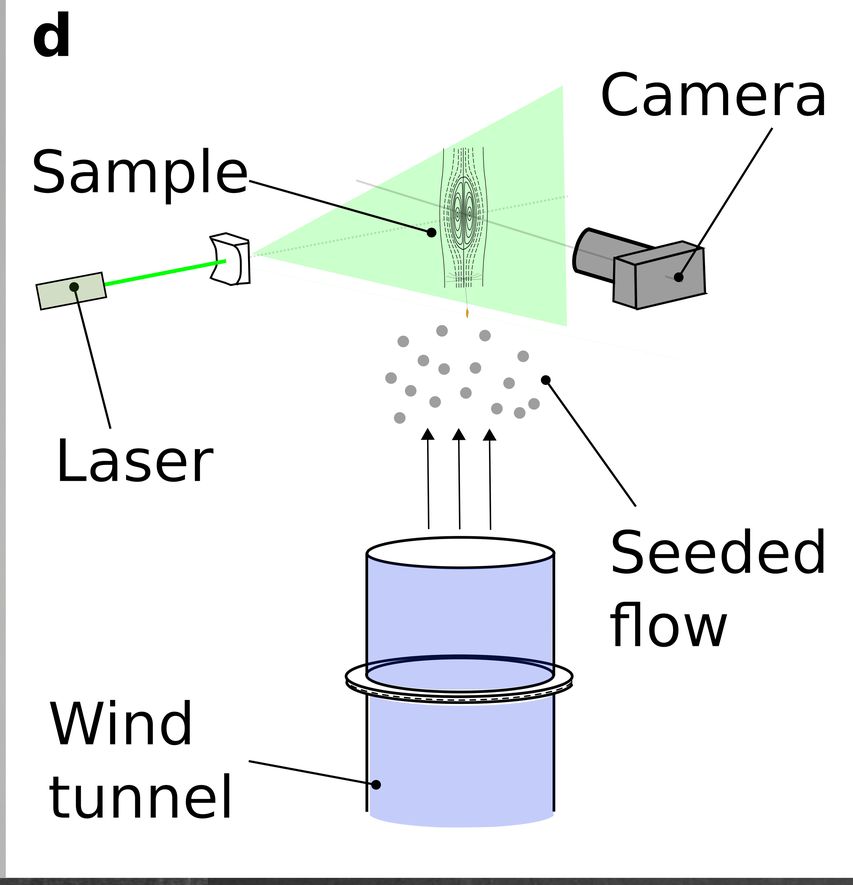
d
Camera
Sample
Laser
Seeded
flow
Wind
tunnel

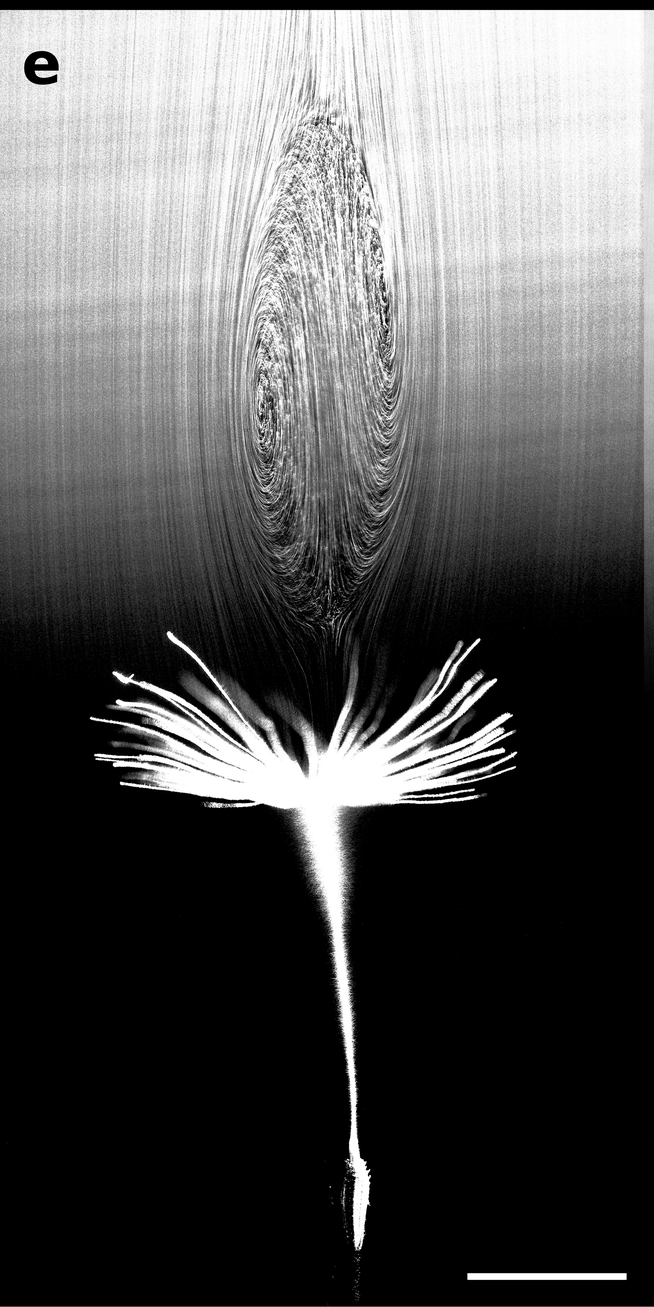
e

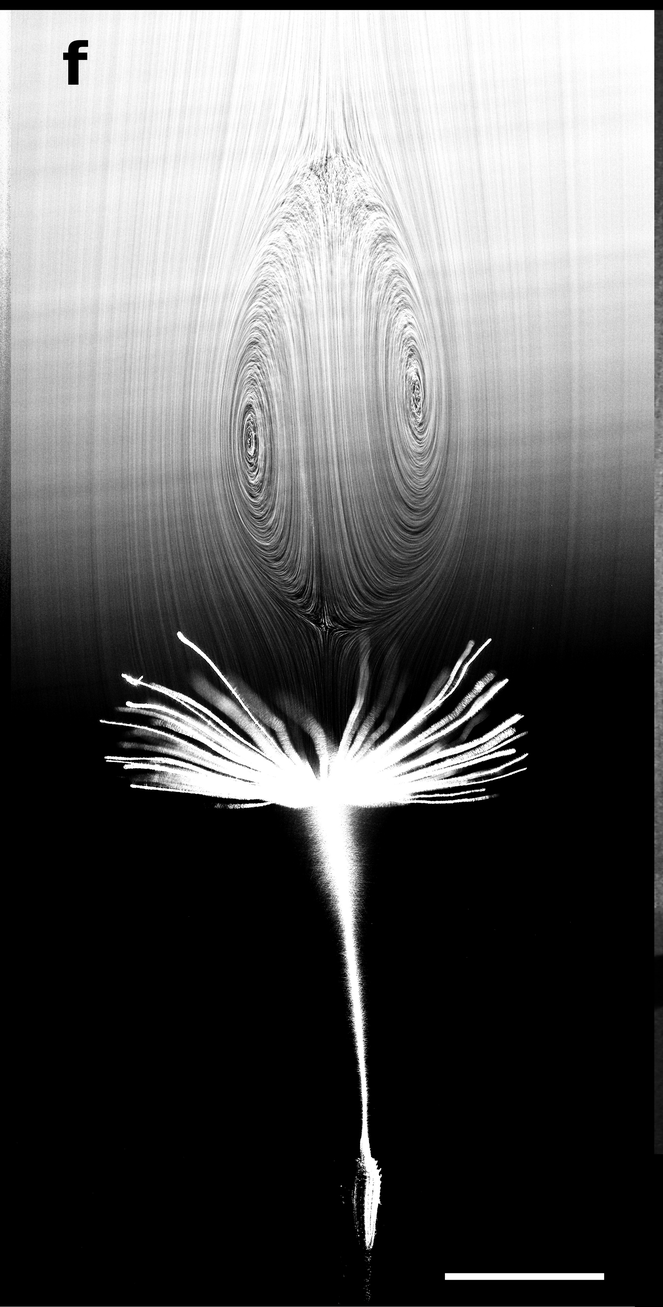
f

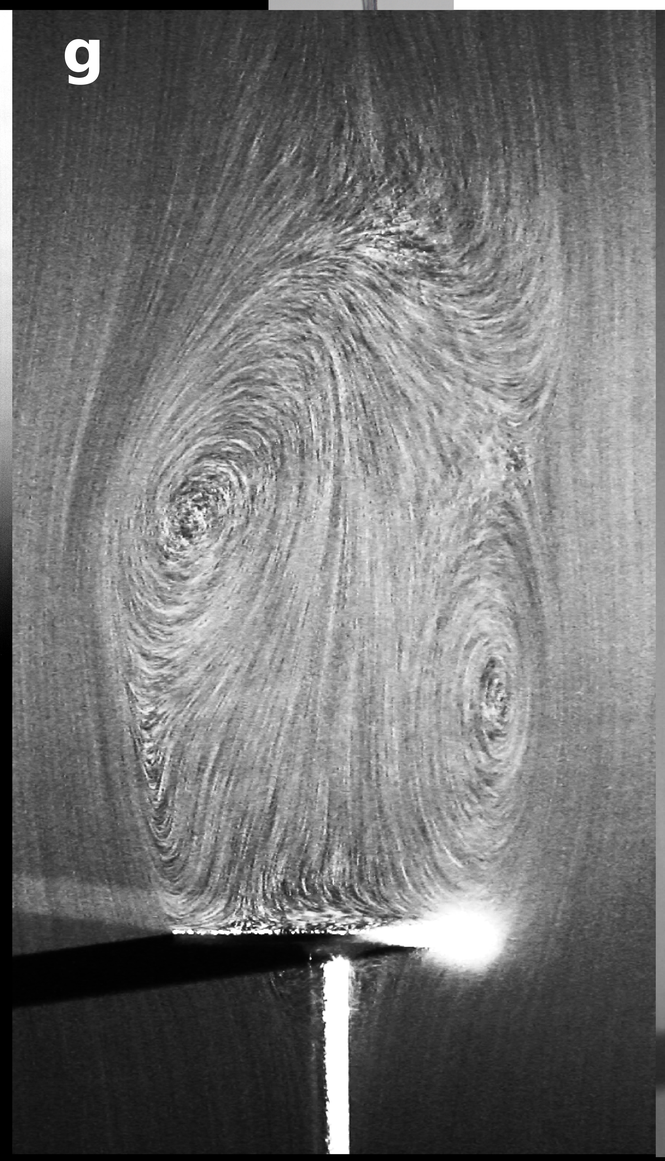
g

h

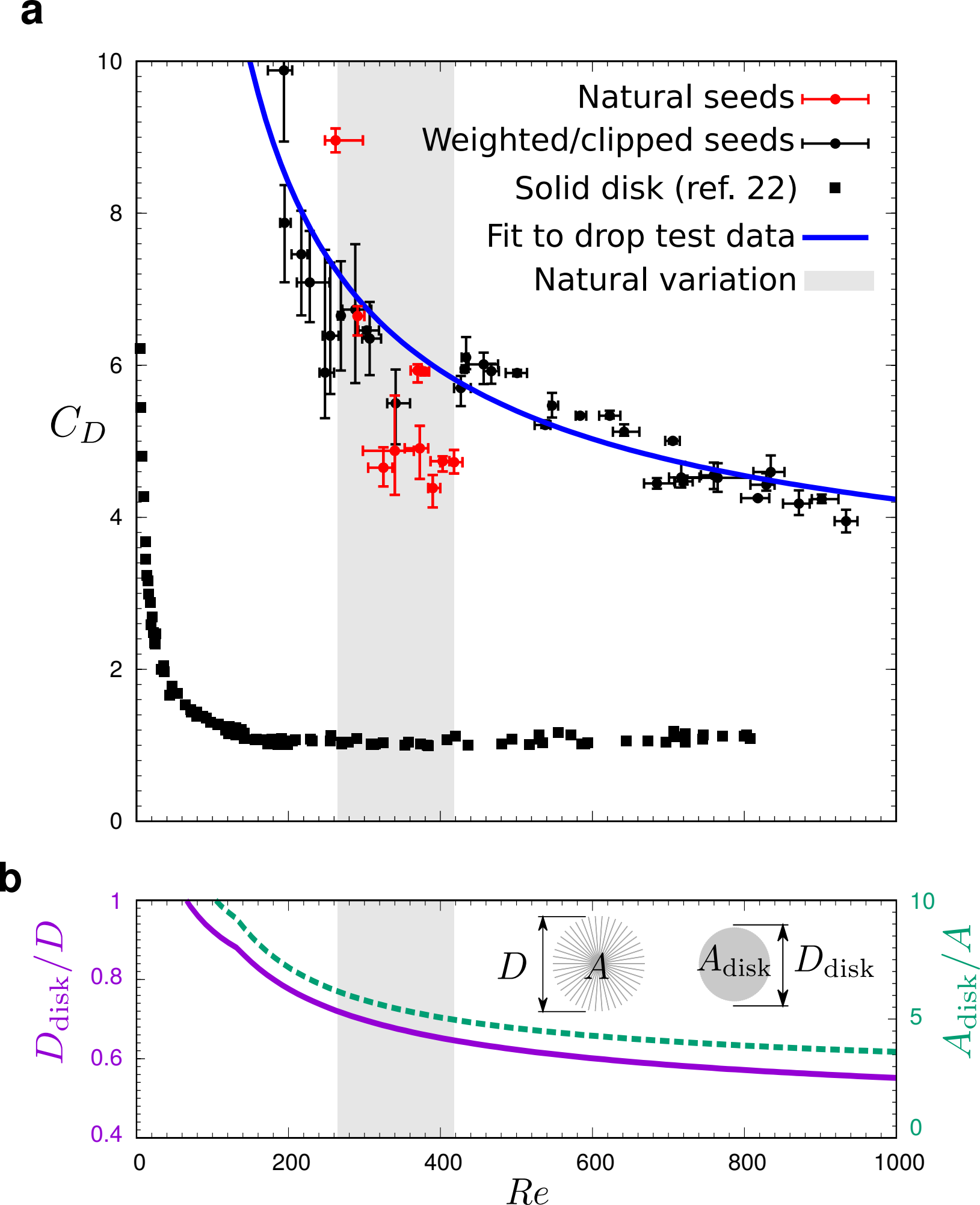
a
b
Natural seeds
Weighted/clipped seeds
Solid disk (ref. 22)
Fit to drop test data
Natural variation
C_D
D_{disk}/D
A_{disk}/A
Re
D
A
A_{disk}
D_{disk}
0
2
4
6
8
10
0.4
0.6
0.8
1
0
5
10
0
200
400
600
800
1000

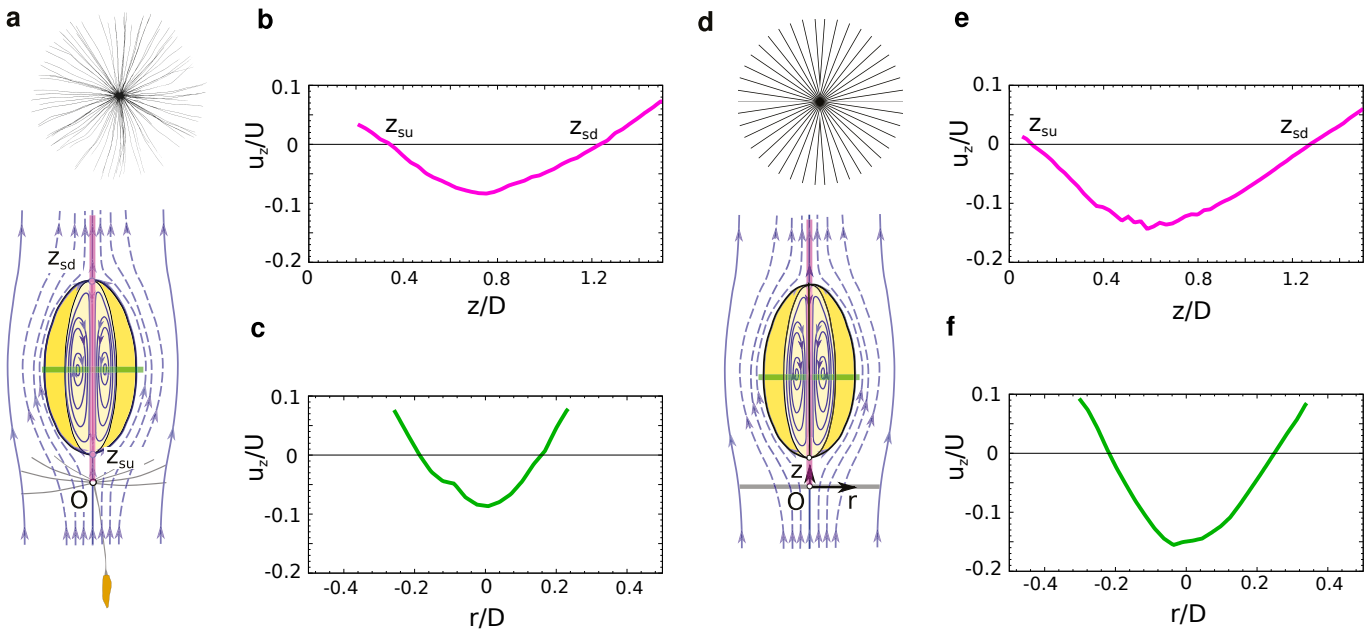
a
b
c
d
e
f
z_{sd}
z_{su}
O
r
u_z/U
z/D
r/D
0.1
0
-0.1
-0.2
0
0.4
0.8
1.2
-0.4
-0.2
0.2

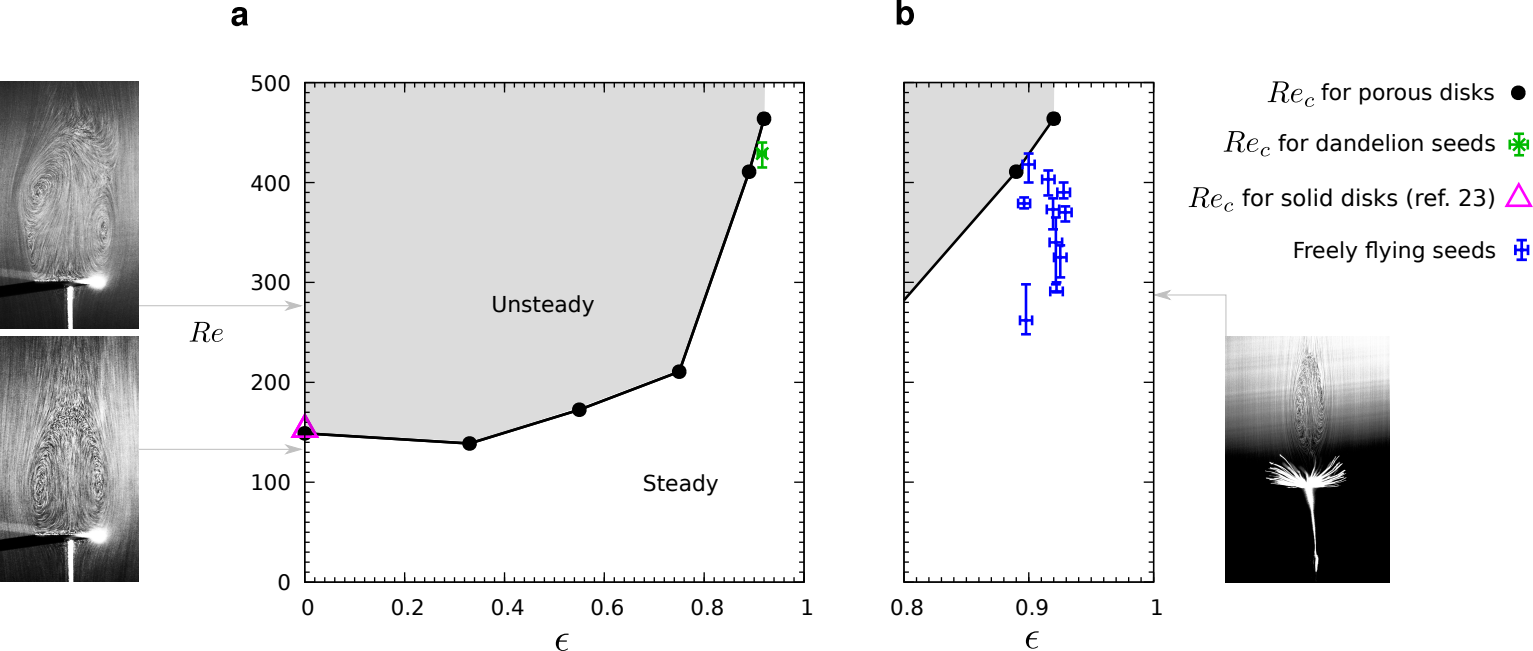
a
b
500
400
300
200
100
0
Re
Unsteady
Steady
0
0.2
0.4
0.6
0.8
1
ϵ
0.8
0.9
1
ϵ
Re_c for porous disks
Re_c for dandelion seeds
Re_c for solid disks (ref. 23)
Freely flying seeds